PHYSICAL REVIEW B VOLUME 51, NUMBER 15 15 APRIL 1995-I

Surface diffusion of H on Ni(100): Interpretation of the transition temperature

Steven E. Wonchoba, Wei-Ping Hu, and Donald G. Truhlar
Department of Chemistry and Supercomputer Institute, University of Minnesota, Minneapolis, Minnesota 55455-0431

(Received 21 July 1994; revised manuscript received 24 October 1994)

We calculate surface-diffusion coefficients for hydrogen on the (100) face of nickel over a temperature range from 40 to 1000 K. The calculations include tunneling contributions from discrete-energy states. The results are in very good agreement with experiment. We find a dramatic leveling off of the Arrhenius plot at approximately 66 K, below which temperature the diffusion coefficient is virtually independent of temperature. The existence and magnitude of such a transition temperature agrees well with experimental findings and also with previous theoretical work based on path-integral transition-state theory. The present treatment provides insight into the origin of the effect. We evaluate the transition temperature analytically in terms of local quadratic approximations to the potential and find it to correspond approximately to the temperature at which the various low-energy bound-reactant states contribute equally to the diffusion coefficient. The nearly temperature-independent diffusion rate below the transition temperature corresponds to tunneling primarily from the ground state. The analytical expression for the transition temperature depends strongly on the magnitude of the frequency at the top of the potential barrier. We also demonstrate that this transition temperature does not correspond to a transition from over-barrier activated diffusion to tunneling diffusion, which has been previously proposed, and that the surface-diffusion process proceeds largely by a tunneling mechanism even well above the transition temperature.

I. INTRODUCTION

Recent experimental[1-3] and theoretical[4] studies on the low-temperature diffusion coefficient of H on Ni(100) have shown a transition from activated Arrhenius behavior at higher temperatures to a nearly temperature-independent diffusion coefficient at a very low temperature. Lin and Gomer[1] first discovered this transition at approximately 100 K using field-emission fluctuation techniques to measure diffusion coefficients. Zhu and coworkers[2,3] later measured the diffusion coefficients using laser-induced thermal desorption and found the transition to occur at approximately 160 K. Mattsson and coworkers[4] studied the process using path-integral transition-state theory with a potential function obtained by the embedded atom method[5] (EAM) and found qualitatively similar results but with a transition temperature at 40 K. All previous interpretations of the transition temperature have been associated with a change in mechanism from an overbarrier process at high temperature to tunneling diffusion at low temperature.

In the present paper, we report calculations of the surface-diffusion coefficients for this process using canonical variational transition-state theory[6-8] (CVT) with a small-curvature tunneling (SCT) approximation[9-13] based on quantized (Q) reactant states[14] (SCTQ). In particular, we use the centrifugal-dominant small-curvature semiclassical adiabatic ground-state tunneling approximation.[12,13] We use an EAM potential function that accurately reproduces experimental binding energies, frequencies, H-Ni interatomic distances, hydrogen equilibrium distances above the surface, and the barrier height for diffusion on the Ni(100) surface. We use the embedded-cluster method[15,16] to model the surface. In Sec. II we discuss the theoretical methods used, and in Sec. III we present and discuss the results, including a reinterpretation of the transition temperature. Section IV is a summary of the conclusions.

II. THEORY AND COMPUTATIONAL METHODS

A. Dynamics methods

Nickel crystallizes in a face-centered-cubic (fcc) lattice structure, and a schematic for the (100) face is shown in Fig. 1. The surface-diffusion process consists of an H

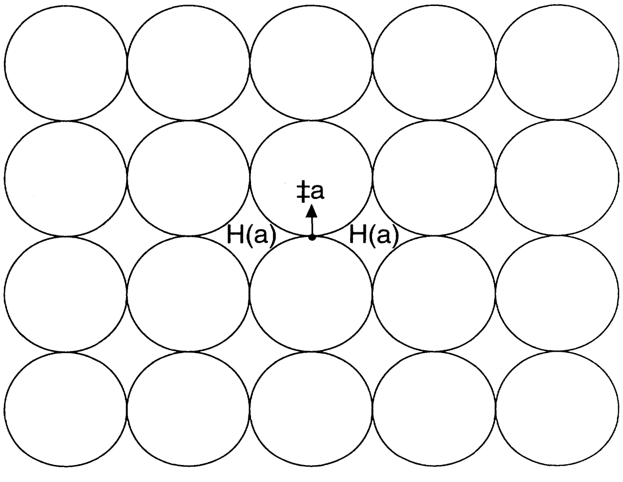

FIG. 1. Schematic diagram of the (100) face of Ni. Two minimum-energy sites of fourfold symmetry are marked H(a), and a saddle point of twofold symmetry is marked by a black dot labeled ‡a. The arrow at the saddle point is a reminder that the saddle point lies higher above the surface plane than do the minimum-energy sites.

atom moving from a fourfold minimum energy site (MES) labeled H(a) in Fig. 1, through a twofold transition state (‡a in Fig. 1), to another fourfold MES. The diffusion coefficient, $D(T)$, is given by

$$D(T)=\frac{\lambda^2}{2d}k^{\mathrm{CVT/SCTQ}}(T)\ , \tag{1}$$

where T is the temperature, λ is the lateral distance between two MES's ($R_0/\sqrt{2}$ for this diffusion process, where R_0 is the lattice constant), d is the dimensionality of the system (two for this and most surface-diffusion processes), and $k^{\mathrm{CVT/SCTQ}}(T)$ is the rate constant determined by CVT with the SCTQ tunneling correction. Equation (1) assumes that the hops between the MES's are uncorrelated, meaning that the H atom remains in the H(a) state long enough to become thermalized and, therefore, have no effect on each subsequent hop.[17]

Equation (1) not only assumes that site-to-site hops for this process are uncorrelated, it also assumes that correlated and multiple jumps contribute negligibly to the diffusion coefficient. Wahnström and co-workers[18] have tested the validity of these assumptions in extensive wave-packet calculations for hydrogen diffusion on a metallic surface, in their case for diffusion on a Cu(100) surface. Their studies indicate that although correlated and multiple jumps are significant for light adatoms (e.g., hydrogen) at very high temperatures, they are much less significant at the lower temperatures, which form the primary focus of the present study. Specifically, for H on rigid Cu(100), their studies showed that correlated and multiple jumps contribute only 7% to the diffusion coefficient at 300 K and only 2% at 200 K. Thus, the neglect of correlated and multiple jump contributions for the present comparison to experimental work is validated to this level of accuracy.

The CVT method has been thoroughly discussed in previous publications (see, for example, Refs. 6–8). We, therefore, only briefly summarize it in the context of the current work. We define a minimum-energy path (MEP) in a mass-scaled coordinate system[19–22] on a potential-energy surface starting at the saddle point and following the path of steepest descents towards the reactant and product MES's. The coordinates are scaled to a reduced mass, μ, of 1 amu. This is an arbitrary value that has no effect on the calculated observables. We define a reaction coordinate, s, along the MEP, where $s=0$ at the saddle point, is negative on the reactant side of the saddle point, and is positive on the product side.

The CVT rate constant is calculated as the equilibrium one-way flux through a dividing surface orthogonal to the MEP. The placement of the dividing surface is variationally optimized so as to minimize the calculated one-way flux and provide a true dynamical bottleneck for the reaction. This is done by maximizing the generalized free energy of activation[8] for the process with respect to s. The position, s, along the MEP at which the variationally optimized dividing surface (the canonical variational transition state) is ultimately placed is called $s_*^{\mathrm{CVT}}(T)$, and the CVT rate constant is defined as

$$k^{\mathrm{CVT}}(T)=\sigma\frac{k_BT}{h}\frac{Q^{\mathrm{CVT}}(T)}{Q^R(T)}\exp\left[\frac{-V_{\mathrm{MEP}}^{\mathrm{CVT}}(T)}{k_BT}\right]\ , \tag{2}$$

where k_B is Boltzmann's constant, h is Planck's constant, σ is a symmetry factor which accounts for the number of equivalent paths from reactants to products for the reaction [four for the (100) surface], $Q^{\mathrm{CVT}}(T)$ and $Q^R(T)$ are the quantized transition state and reactant partition functions, and $V_{\mathrm{MEP}}^{\mathrm{CVT}}(T)$ is the potential energy of the system at the canonical variational transition state [at $s_*^{\mathrm{CVT}}(T)$ along the MEP].

The vibrationally adiabatic ground-state potential-energy curve is defined by

$$V_a^G(s)=V_{\mathrm{MEP}}(s)+\varepsilon_{\mathrm{trans}}^G(s)\ , \tag{3}$$

where $V_{\mathrm{MEP}}(s)$ is the potential energy of the system at s on the MEP, and $\varepsilon_{\mathrm{trans}}^G(s)$ is the sum over all vibrational modes orthogonal to the reaction coordinate of the zero point energies at s. Here and throughout this paper, G denotes the ground state of modes transverse to the reaction coordinate. (This should not be confused with the ground state of the motion from the initial minimum-energy site *along the reaction coordinate,* which will play a prominent role below.) For the processes in this study, there are a total of (N_p+1) moving atoms (N_p moving nickel atoms and one hydrogen atom), which contribute vibrational energy to the system. This yields $F=3N_p+3$ vibrational normal modes (there are no unbound translations or rotations for a substrate-surface reaction or for surface diffusion processes) for the reactant, and $F-1$ transverse modes for the generalized transition state.

The minimum-potential-energy curve, $V_{\mathrm{MEP}}(s)$, decreases monotonically from $s=0$ to s^R, where s^R is the value of s at the reactant MES. Thus, $V_{\mathrm{MEP}}(s^R)$ is the classical global minimum of energy. However, in the present case, the vibrationally adiabatic ground-state potential-energy curve has a nonmonotonicity in the region of $s=s^R$. To understand why this occurs, we observe the character of the orthogonal modes that contribute to $\varepsilon_{\mathrm{trans}}^G(s)$. Of the F vibrational modes in this process, $F-3$ modes are low-frequency lattice vibrations, and three modes are high-frequency hydrogenic vibrations. The vibrational modes are numbered starting with the highest vibrational frequency (mode 1) down to the lowest vibrational frequency (mode F). At this point, we single out two particularly important vibrational modes. Mode 3, with vibrational frequency $\bar{v}_3$ in wave numbers, is the lowest-frequency hydrogenic vibration, and mode F, with vibrational frequency $\bar{v}_F$ in wave numbers, is the overall lowest-frequency vibration. These two modes trade character over the course of the reaction path, causing the vibrationally adiabatic ground-state curve to decrease nonmonotonically from the transition state to the reactant. Specifically, at the generalized transition state, $F-3$ of the transverse modes are low-frequency lattice vibrations, and the remaining two transverse modes are high-frequency modes due to hydrogenic vibration. The mode corresponding to the reaction coordinate is mode 3, the lowest-frequency hydrogenic vibration. Over the course of the reaction path, however, the character of the reaction coordinate changes, becoming less and less hydrogenic in character. Finally, as s is very nearly equal to s^R, the mode corresponding to the reaction coordinate is almost completely mode F, the overall lowest-frequency vibration, and there are $F-4$ transverse low-frequency lattice vibrations and three transverse high-frequency vibrations. As a result, the V_a^G curve reaches a minimum at the point at which the reaction coordinate mode has lost its hydrogenic attributes, and it has a local maximum at $s=s^R$. For the process studied in this paper, N_p is 36, and F is 111. Figure 2 shows the $V_{\mathrm{MEP}}(s)$ and $V_a^G(s)$ curves with two independent scales (given on the left and right) for the ordinate to account for the difference in energetic magnitude of the two quantities. The double minimum only occurs in the $V_a^G(s)$ curve, indicating that this feature is exclusively a result of the transverse modes [see Eq. (3)]. This double well considerably complicates the dynamics calculations. This is discussed below.

In Eq. (2), all modes are treated quantum mechanically except for motion along the reaction coordinate. To quantize the reaction coordinate, k^{CVT} is multiplied by a ground-state transmission coefficient, $\kappa^{\mathrm{CVT}/G}$, which accounts for the tunneling along the reaction path (where again G denotes the ground state of the transverse modes). The transmission coefficient is the ratio of the Boltzmann-averaged quantum transmission probability across the $V_a^G(s)$ barrier to the Boltzmann-averaged classical transmission probability across the same barrier. The denominator must be consistent with CVT, for which the implicit threshold energy (i.e., the energy above which the probability for transmission is unity and below which it is zero) is $V_a^G(s=s_*^{\mathrm{CVT}}(T))$. This gives the following expression for the ground-state transmission coefficient at the CVT level:[23]

$$\kappa^{\mathrm{CVT/G}}(T)=\frac{\int_0^\infty dE\,P^G(E)\exp(-E/k_BT)}{\int_{V_a^G(s=s_*^{\mathrm{CVT}}(T))}^\infty dE\,\exp(-E/k_BT)}\,, \tag{4}$$

where $P^G(E)$ is the quantum transmission probability defined by

$$P^G(E)=1/\{1+\exp[2\theta(E)]\}\,, \tag{5}$$

where $\theta(E)$ is the imaginary action integral[8-10] for the barrier transmission and depends upon the tunneling approximation used. When Eq. (4) is used to quantize the reaction path, the final rate constant, i.e., the product of Eqs. (2) and (4), is denoted $k^{\mathrm{CVT/SCT}}$.

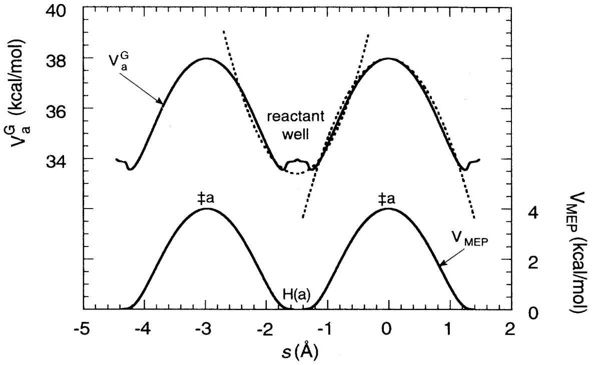

FIG. 2. Vibrationally adiabatic ground-state and MEP potential-energy curves for surface diffusion. The left-hand ordinate is the energy, in kcal/mol, of the V_a^G curve. The right-hand ordinate is the energy of the V_{MEP} curve. The abscissa is s, the reaction coordinate. The saddle point, ‡a, from which the MEP is started is at $s=0$, and the reactant MES, H(a), is at $s^R=-1.48$ Å. For $s<s^R$, the curves are defined by a reflection around s^R, resulting in a double minimum in the reactant well of the V_a^G curve. See Sec. II A for further discussion. The dotted parabolic curve in the vicinity of the reactant well of the V_a^G curve is the harmonic approximation to the curve, which is used to obtain the harmonic energy eigenstates, E_v^R. The dotted parabolic curve in the vicinity of the saddle point represents the parabolic approximation to the curve which is used to obtain approximate transmission probabilities, $P^G(E_v^R)$.

When a particle tunnels through a barrier from a well, as is the case for the current problem of an H atom diffusing across a surface between minimum-energy sites, it initially occupies discrete energy levels in the well, and each site-to-site hop originates from a discrete energy state rather than from an energy drawn from the continuum, as implied by Eq. (4). Under most (high-temperature) conditions we can ignore this discreteness, but at low temperatures it becomes very important. We, therefore, define a ground-state (G) transmission coefficient with a quantized (Q) reaction-coordinate state, called GQ, in which contributions to the rate process from all discrete well levels below the maximum of the V_a^G curve, called V_a^{AG}, are summed individually. Therefore, in Eq. (4), only energies above V_a^{AG} are treated as a continuum, and the GQ transmission coefficient becomes

$$\kappa^{\mathrm{CVT/GQ}}(T)=\frac{\sum_{v=0}^{M}\frac{dE_v^R}{dv}P^G(E_v^R)\exp(-E_v^R/k_BT)+\int_{V_a^{\mathrm{AG}}}^\infty dE\,P^G(E)\exp(-E/k_BT)}{\int_{V_a^G(s=s_*^{\mathrm{CVT}}(T))}^\infty dE\,\exp(-E/k_BT)}\,. \tag{6}$$

The upper limit, M, of the summation is the total number of well eigenenergies, E_v^R, below V_a^{AG}. We evaluate the quantized energy of the mode corresponding to the reaction path in the WKB approximation, and the well eigenenergies are solutions to the well-known Bohr-Sommerfeld quantization condition:

$$\int_{s_-}^{s_+} ds\sqrt{2\mu[E_v^R-V_a^G(s)]}=\frac{h}{2}(v+\tfrac{1}{2})\,, \tag{7}$$

where s_+ and s_- are the classical turning points, such that $s_- < s^R < s_+ < 0$.

The definition of the adiabatic ground-state potential energy curve in Eq. (3) applies only for s greater than s^R since the minimum energy path is only calculated from the saddle point down to the reactant minimum-energy well. To apply Eq. (7), the back side of the vibrationally adiabatic ground-state potential-energy curve, i.e., $V_a^G(s)$ for s less than s^R, is needed as well. There is no unique way of specifying this part of the potential for general unimolecular reactions. For the reaction in the current study, however, the metallic surface is periodic, and the potential profile is symmetric about a given MES. Therefore, $V_a^G(s)$ for s less than s^R is simply determined by reflection of the known part of the adiabatic potential (see Fig. 2), and Eq. (7) is solved numerically to get E_ν^R.

To obtain $dE_\nu^R/d\nu$ for use in Eq. (6), we fit the energy eigenstates to a quadratic equation,

$$E_\nu^R = a\nu^2 + b\nu + c \ , \tag{8}$$

which yields

$$\frac{dE_\nu^R}{d\nu} = 2a\nu + b \ . \tag{9}$$

For the lowest and highest ν, we base the fit on the lowest and highest three levels, whereas for the intermediate ν we base the fit on levels $\nu - 1$, ν, and $\nu + 1$. Note that this technique is only possible when at least three energy levels are open below V_a^{AG}.

Since we use the WKB approximation for the reaction-path mode, we must, for consistency, evaluate the reactant partition function, $Q^R(T)$, with the WKB energy levels for this mode. The reactant partition function is given by the usual separable mode form as

$$Q^R(T) = \prod_{m=1}^{F} \left[\sum_{\nu=0}^{\infty} \exp\left[\frac{-\varepsilon_\nu^{R,m}}{k_B T} \right] \right] , \tag{10}$$

where $\varepsilon_\nu^{R,m}$ is the vibrational energy of level ν of mode m of the reactant, the reaction coordinate mode is calculated with the WKB energy levels, and all other modes are calculated with the harmonic energy levels. The fact that the nature of the reaction coordinate changes over the course of the reaction path presents a significant complication. The complication occurs due to the double well (discussed above, see Fig. 2) that occurs in the V_a^G curve in the proximity of $s = s^R$. In order to motivate our treatment of this complication as well as to provide a qualitative basis for understanding our results, we first consider a global harmonic approximation to the potential in the well, namely,

$$V_a^G(s) \approx V_a^G(s = s^R) + \tfrac{1}{2}hc(\bar{\nu}_F^R - \bar{\nu}_3^R) + \tfrac{1}{2}f_3(s - s^R)^2 \ , \tag{11}$$

where $\bar{\nu}_F^R$ is the frequency in wave numbers of mode F at $s = s^R$ (at which point mode F corresponds to the reaction coordinate), and $\bar{\nu}_3^R$ is the frequency in wave numbers at $s = s^R$ of mode 3 (which corresponds to the reaction coordinate over most of the reaction path away from $s = s^R$), f_3 is the force constant corresponding to this mode, and c is the speed of light. The well levels computed from this effective potential are

$$E_\nu^R \approx V_a^G(s = s^R) + \tfrac{1}{2}hc\bar{\nu}_F^R + \nu hc\bar{\nu}_3^R \ , \tag{12}$$

where ν is a non-negative integer. Therefore,

$$\frac{dE_\nu^R}{d\nu} \approx hc\bar{\nu}_3^R \ . \tag{13}$$

Since Eqs. (11) through (13) show that the reaction coordinate has the character of mode F over a small path of its range (i.e., for s very close to s^R) and of mode 3 over the rest, it is not physical to simply calculate modes 1 through $F-1$ using harmonic energy levels with frequencies $\bar{\nu}_1$ through $\bar{\nu}_{F-1}$ and then calculate mode F (the low-frequency lattice vibration, which corresponds to the reaction coordinate at $s = s^R$) using WKB energy levels, because that would effectively include mode 3 twice since the energy separations in the reaction coordinate more accurately reflect mode 3 as discussed previously. Conversely, it is also not physical to treat mode 3 as the reaction-path mode, because mode 3 is transverse to the reaction coordinate at $s = s^R$. We need to calculate the partition function such that the ground-state energy is accurate at $s = s^R$ and the energy spacings are accurately represented. To do this, we recognize that two modes have mixed character and we replace Eq. (10) by

$$Q^R(T) = Q_{3,F}^R(T) Q_{F,3}^R(T) \prod_{\substack{m=1 \\ m \neq 3}}^{F-1} Q_m^R(T) \ , \tag{14}$$

where $Q_{3,F}^R(T)$ and $Q_{F,3}^R(T)$ are the partition functions of the mixed modes, and $Q_m^R(T)$ are the partition functions of the separable modes. The $Q_m^R(T)$ are calculated harmonically in the usual way, and we now consider the mixed modes. The first quantity in Eq. (14) is a harmonic mixture of mode 3 and mode F and is approximated by

$$Q_{3,F}^R(T) = \sum_{\nu=0}^{\infty} \exp\left[-hc \left[\frac{\bar{\nu}_3^R}{2} + \nu \bar{\nu}_F^R \right] \Big/ k_B T \right] . \tag{15}$$

This function has the zero-point energy of mode 3 and the energy spacing of mode F. The second quantity in Eq. (14) is a WKB treatment of the reaction coordinate, combining mode F with the WKB energy levels determined by Eq. (7). This quantity is given by

$$Q_{F,3}^R(T) = \sum_{\nu=0}^{\infty} \exp\left[-\left[hc\frac{\bar{\nu}_F^R}{2} + E_\nu^R - \Delta\varepsilon \right] \Big/ k_B T \right] , \tag{16}$$

where $\Delta\varepsilon$ is equal to the total zero-point energy of the reactant calculated from the harmonic approximation to all the modes, i.e.,

$$\Delta\varepsilon = \sum_{m=1}^{F} \tfrac{1}{2}hc\bar{\nu}_m^R \ . \tag{17}$$

Several methods have been developed to approximate $P^G(E)$.[8–13,23–25] Tunneling in systems with zero curvature along the reaction path is well approximated with a ZCT (zero-curvature tunneling) algorithm, which assumes that the tunneling path coincides with the reaction path and uses the MEP as the tunneling path.[11,24] Tunneling in systems with large curvature along the reaction path may be approximated by the large-curvature-version-3 (LCG3) method,[13,25] and for systems with small curvature along the reaction path, we use the SCT tunneling approximation (more completely labeled CD-SCSAG, for centrifugal-dominant small-curvature semiclassical adiabatic ground-state approximation).[12] The ground-state transmission coefficients for the ZCT, LCG3, and SCT tunneling approximations were compared, and the SCT approximation always gave the largest transmission coefficient, indicating that the tunneling process is most accurately represented by an approximation that assumes small curvature along the reaction path. Thus, all results presented in this paper were calculated with the SCT tunneling approximation combined with quantized reaction-coordinate states, which will be called the SCTQ approximation.

In the SCTQ and SCT approximations,[12,13] the imaginary action integral in Eq. (5) is given by

$$\theta(E)=(2\pi/h)\int_{s_0}^{s_1} ds\sqrt{2\mu_{\text{eff}}(s)[V_a^G(s)-E]} \ , \tag{18}$$

where s_0 and s_1 are the limits of the tunneling path, and μ_{eff} is an effective reduced mass which accounts for reaction-path curvature in all normal modes. The calculation of μ_{eff} is fully discussed elsewhere.[12(a),13]

The quantized well method has been used in previous work[14] to calculate hydrogen diffusion coefficients on Cu(100), but since these calculations were not made at extremely low temperatures, the excited-state population was never negligible, and quantizing the reactant states did not produce results appreciably different from the original continuum calculation. In the current work, the quantization makes a very noticeable difference in the very low-temperature region (below 70 K).

B. Potential-energy function

For a system with only one nonmetal atom, as in the current work, the total potential energy of the system, V, is estimated by the EAM formalism[5,26] as

$$V=\sum_i\left[F_i(\bar{\rho}_i)+\frac{1}{2}\sum_{j\neq i}\phi_{ij}(R_{ij})\right] \ , \tag{19}$$

where the sums are over all atoms, and R_{ij} is the internuclear distance between atoms i and j. Each term in the summation over i is a sum of two terms. The first term, $F_i(\bar{\rho}_i)$, called the embedding energy, is the energy to embed atom i into a surrounding electron density, $\bar{\rho}_i$, where

$$\bar{\rho}_i=\sum_{j\neq i}\rho_j^a(R_{ij}) \tag{20}$$

is the sum of the electron densities of all the other atoms j at the location of atom i. The individual electron-density contributions of each Ni atom are taken from single determinant Hartree-Fock wave functions as

$$\rho_j^a(R_{ij})=N_s\rho_s(R_{ij})+(N-N_s)\rho_d(R_{ij}) \quad (j=\text{Ni atom}) \ , \tag{21}$$

where N is the number of valence shell electrons (10 for Ni) and N_s is the effective number of s electrons (2 for these calculations), and ρ_s and ρ_d are the spherically averaged s- and d-like atomic densities described by Daw and Baskes.[5] The contribution from the H atom is taken as the electron density of the 1s shell,

$$\rho_j^a(R_{ij})=\frac{\exp(-2R_{ij}/a_0)}{\pi(a_0)^3} \quad (j=\text{H atom}) \ , \tag{22}$$

where a_0 is the bohr radius. The embedding functions for hydrogen and nickel have the functional forms given in previous work:[27]

$$F_{\text{H}}(\rho)=\alpha_{\text{H}}\rho\exp(-\beta_{\text{H}}\rho) \tag{23}$$

and

$$F_{\text{Ni}}(\rho)=\begin{cases}A\rho\exp(-\alpha\rho)+B\rho^3\exp(-\beta\rho)+C\rho\exp(-\gamma\rho), & 0\leq\rho\leq\rho_c-\Delta\\ A_s(\rho-\rho_c)^5+B_s(\rho-\rho_c)^4C_s(\rho-\rho_c)^3+D_s, & \rho_c-\Delta<\rho\leq\rho_c\\ D_s, \ \rho_c<\rho \ , & \end{cases} \tag{24}$$

where the coefficients are determined semiempirically.

The second term in Eq. (19) is a repulsive pair potential, ϕ_{ij}, and is defined as a Coulomb interaction,

$$\phi_{ij}(R_{ij})=\frac{C_\phi Z_i(R_{ij})Z_j(R_{ij})}{R_{ij}} \ , \tag{25}$$

where C_ϕ is a constant, and $Z(R_{ij})$ is the effective charge for atom i or j and has the functional form taken from Foiles, Baskes, and Daw,[28]

$$Z(R)=Z_0(1+bR^c)\exp(-aR) \ , \tag{26}$$

where Z_0, a, b, and c are determined semiempirically. To establish a cutoff for the electron-density contributions and the pair potential, $\rho_j^a(R_{ij})$ in Eqs. (21) and (22) and $Z(R_{ij})$ in Eq. (26) are multiplied by a smoothing function, $s(R)$, which has the form defined in previous work:[29]

$$s(R)=\begin{cases} 1, \quad R \le R_c \\ \dfrac{R-(R_c+\Delta)}{-\Delta}-\dfrac{1}{2\pi}\sin\left[\pi\left[\dfrac{2R-2R_c-\Delta}{\Delta}\right]\right], \quad R_c < R < R_c+\Delta \\ 0, \quad R_c+\Delta \le R \ , \end{cases} \tag{27}$$

where R_c and Δ are chosen to be large enough to yield a smooth potential cutoff.

There have been several parametrizations of EAM for H/Ni to reproduce various experimental quantities. Originally, Daw and Baskes[5] presented a parametrization (we will call this EAM1) for hydrogen dissolution in bulk nickel, which was fit to bulk parameters such as the elastic constants (C_{11}, C_{12}, and C_{44}), the monovacancy formation energy (E_{IV}^F), and the sublimation energy (E_S). Another parametrization, called EAM2 in the present paper, was presented by Rice *et al.*[30] Their goal was to improve the parameters so that hydrogen on the surface of nickel is also treated accurately. The third and fourth EAM parameter sets were proposed in conjunction with embedded diatomics in molecules (EDIM), a method developed to treat multiple adatoms on a Ni surface. EAM3, presented by Truong, Truhlar, and Garrett[27] changed the embedding function for nickel from a spline fit to an analytical function, changed the form of the hydrogen embedding function to eliminate unphysical results in the high-density region, and enabled the potential routine to handle steps along the metal surface. EAM4 (Ref. 29) involved minor modifications to the smoothing function [yielding the current smoothing function, Eq. (27)]. It also involved some adjustments to allow calculations for three adatoms on a Ni surface. The EAM4 function gives a reasonable potential-energy surface for many aspects of the H adatom dynamics, but it does not predict accurate values for E_{IV}^F, E_S, and R_0 [where the latter is the equilibrium bulk lattice constant, which is 3.52 Å (Ref. 31)]. Since we intend to study subsurface dynamics in a later work, it is desirable that the potential function accurately predict these bulk quantities as well as the surface quantities (hydrogen vibrational frequencies, hydrogen-nickel equilibrium distances, and surface binding energies).

In order to improve this situation, we made further changes to the potential parameters to obtain a potential function that we call EAM5. We started with the EAM4 Ni embedding function parameters of Eq. (24) and fine tuned them by fitting the embedding function as closely as possible to a set of embedding energies calculated by the equation of state of nickel,[32] over a range of densities, ρ, as was done in the spline fit of Rice *et al.*[30] It is not necessary, however, to attempt a global fit of Eq. (24) to these energies over the entire range of densities because there are some regions of the density range which are more important for the process at hand than others. In particular, the equilibrium densities felt by the lattice atoms (both surface and bulk atoms) at the stationary points of the reaction path (i.e., the minimum-energy sites and saddle points) are very important because the resulting embedding energies calculated at these densities greatly affect the energetics of the stationary points. Similarly, the densities felt by the lattice atoms over the course of the reaction path are very important in order to accurately reflect the energies of the reaction path and produce a realistic MEP. As a result, we paid particular attention to the equilibrium atomic densities, $\bar{\rho}$, of the lattice atoms at all the stationary points of interest for the present study.

The first row of Table I lists $\bar{\rho}$, defined in Eq. (20), for bulk Ni atoms and (100) surface atoms when no adatom is present. For the surface Ni atom calculations, 36 atoms in the vicinity of the surface (chosen as those surrounding two adjacent first-subsurface-plane octahedral

TABLE I. Atomic densities $\bar{\rho}_i$ (Å^{-3}) at the positions of surface and bulk Ni atoms for the case of a nonrigid system. NC indicates that the adsorbed atom does not change $\bar{\rho}_i$ for the Ni atom in question. Numbers in parentheses are the number of equivalent atoms to which the altered $\bar{\rho}_i$ applies.

		$\bar{\rho}_i$	
Situation	Footnote	(100) surface atom	Bulk atom
Clean surface	a	0.0445	0.0670
H atom at H(a)	b	0.0459 (4)	NC
H atom at ‡a	b	0.0500 (2)	NC
H atom at O_b	c	NC	0.0666–0.0673 (32)
H atom at ‡OT	d	NC	0.0649–0.0691 (19)

[a] H atom infinitely separated from the surface.

[b] H(a) and ‡a are defined in Fig. 1.

[c] H atom adsorbed in an octahedral vacancy in the bulk.

[d] H atom adsorbed at a saddle point between octahedral and tetrahedral vacancies in the bulk.

TABLE II. Parameter set for EAM5.

Parameters for ρ_{Ni}	$N_s=2$	$N=10$		
Parameters for F_{H}	$\alpha_{\mathrm{H}}==70.5461$ eV Å^3	$\beta_{\mathrm{H}}=6.9507$ Å^3		
Parameters for F_{Ni}	$A=-126.5009308$ eV Å^3	$\alpha=0.3362141252$ Å^3	$B=6033.287109$ eV Å^9	$\beta=11.02211666$ Å^3
	$C=-209.7682800$ eV Å^3	$\gamma=51.76818085$ Å^3	$\rho_c=0.21$ Å^{-3}	$\Delta=0.01$ Å^{-3}
	$A_s=-1.657208422\times10^{10}$ eV Å^{15}	$B_s=-5.13226816\times10^{8}$ eV Å^{12}	$C_s=-4.377938\times10^{6}$ eV Å^9	$D_s=-19.23463058$ eV
Parameter for ϕ	$C_\phi=14.3888$ eV Å			
Parameters for Z_{H}	$Z_0=0.1959$	$a=1.7957$ Å^{-1}	$b=3.2108$ Å^{-1}	$c=1.0$
Parameters for Z_{Ni}	$Z_0=10.0$	$a=1.8633$ Å^{-1}	$b=0.8957$ Å^{-1}	$c=1.0$
Parameters for s	$R_c=5.0$ Å	$\Delta=5.0$ Å		

vacancies as described in the following section) were allowed to relax. For the bulk atom calculations, 52 atoms (chosen as those surrounding two adjacent bulk octahedral vacancies) were allowed to move. When a H atom comes in contact with the lattice, it slightly changes $\bar{\rho}$ for a small number of Ni atoms (i.e., a subset of those atoms allowed to relax) that are in close proximity it. The subsequent rows of Table I list $\bar{\rho}$ for the Ni atoms that are most affected when a H atom is adsorbed or absorbed at various sites. As a result, given the information in Table I, the only data used for fitting Eq. (19) were the selected values of the embedding energies of Ref. 32 in the density ranges from 0.0445 to 0.0500 Å^{-3} and from 0.0649 to 0.0691 Å^{-3}. These density ranges sufficiently cover the densities at each of the Ni lattice atom sites over the course of the various processes that are to be studied with EAM5. We then carried out the parametrization with the goal to make R_0 accurate to within 0.01 Å (for reasons made clear in Ref. 16, R_0 is very important for tunneling calculations) and to improve the accuracy of E_{IV}^F and E_S.

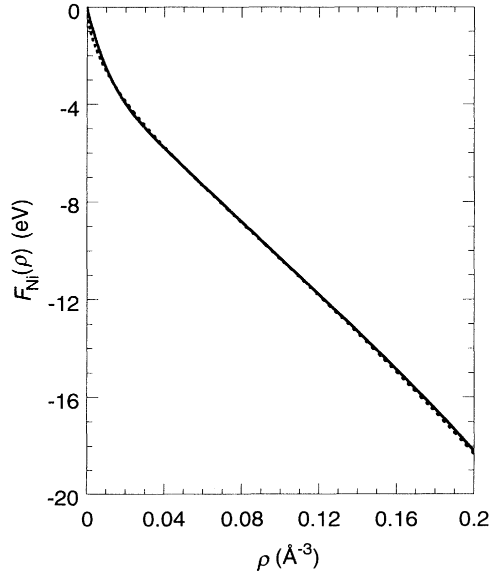

FIG. 3. Ni embedding function vs density. The solid line corresponds to the EAM5 parameter set using Eq. (24). The dotted line corresponds to the set of values determined from the equation of state of Ni as in Rose *et al.* (Ref. 32).

The final EAM5 Ni embedding function is plotted with the energies of Ref. 32 in Fig. 3. All other functions in the parameter set are identical to those in EAM4.[29] The EAM5 parameter set is given in Table II, and Table III lists the bulk quantities calculated using EAM5 and compares them to experiment[31,33–38] and to calculations using EAM4.[29] Some other EAM formulations[28] use the equation of state of nickel[32] directly to calculate the embedding function. In the current work, however, the EAM potential is being used to make dynamics calculations. For computational efficiency and stability in such applications, we want the embedding energy to be represented as an analytical function of the density with continuous first and second derivatives. This is especially important for calculating the minimum-energy path and the frequencies and V_a^G curves along it. We believe that EAM5 is adequate for the studies presented here and is a good starting point for later studies including subsurface H below the (100) surface because it yields an accurate value for the experimental lattice constant and because the Ni embedding energy is an analytical function.

C. Details of the lattice

The nickel system is modeled by the embedded-cluster method.[15,16] The lattice is taken large enough to include

TABLE III. EAM5 calculated values for equilibrium bulk lattice constant (Å), monovacancy formation energy (eV), sublimation energy (eV), and elastic constants (10^{12} dyn/cm^2) compared to EAM4 calculations and to experiment.

Quantity	Experiment	EAM4	EAM5
R_0	3.52[a]	3.54	3.5211
E_{IV}^F	1.39–1.70[b]	1.78	1.66
E_S	4.45[c]	4.22	4.43
C_{11}	2.465[d]	1.914	1.852
C_{12}	1.473[d]	1.244	1.238
C_{44}	1.247[d]	1.294	1.255

[a] Reference 31.
[b] References 34–37.
[c] Reference 38.
[d] Reference 33.

all the variable interactions for all atoms that may be made movable (i.e., as far as the potential cutoff in all directions from all potential movable atoms). The lattice for these studies on the (100) surface consists of 666 atoms: 100, 98, 100, 98, 78, 78, 58, 38, and 18 atoms in the first through ninth planes descending down perpendicular to the (100) surface. The lattice is constructed with the energetically minimized lattice constant, 3.5211 Å (see Table III).

Calculations are made for a system in which several atoms near the site of the diffusion process are allowed to move. As in previous work,[16] the atoms allowed to move are chosen as those which fall into the confines of dual spheres of equal radii, which are centered near the reactant and product sites. We eventually plan to combine the current work on surface diffusion with a larger project to involve hydrogen atom infusion beneath a surface and subsurface diffusion, so the centers of the spheres are chosen in such a way as to accommodate all processes to be eventually studied so that all processes can be related and treated in identical environments. Thus, for the (100) surface, the spheres are centered at two adjacent octahedral vacancies immediately beneath the two adjacent surface atoms, which are nearest neighbors to the ‡a site in Fig. 1, and the embedded cluster of moving atoms consists of 36 atoms: 12, 16, and 8 atoms in the first through third planes. Consistent with the discussion below Eq. (3), we will, throughout this paper, use the variable N_p to define the number of moving atoms in the embedded cluster. Since, as will be discussed in the following section, lattice motion had almost negligible effects on the energetics and dynamics of these surface processes [we performed calculations on a rigid ($N_p=0$) system, and the results were qualitatively similar to those of the moving ($N_p=36$) system], we restrict our presentation of results to the moving ($N_p=36$) system unless otherwise noted.

III. RESULTS AND DISCUSSION

A. Energetics and vibrational frequencies

We present calculated binding energies, hydrogen-nickel equilibrium interatomic distances, hydrogen equilibrium distances from the surface plane, and hydrogen vibrational frequencies for an adatom adsorbed at each of the sites on the (100) surface and compare them to experimental and other calculated values[4,41–51] in Table IV. A summary of the thermodynamics involved in determining the experimental equilibrium binding energies is presented in Appendix A. The H(a) binding energies, frequencies, hydrogen equilibrium distances above the surface, and H-Ni equilibrium distances are in very good agreement with experiment. Activation energies can be calculated directly from rate constant data, and this will be done in the following section and shown to lead to very good agreement with experiment. However, our calculations indicate that the classical barrier height (4.00 kcal/mol) is very close to the high-temperature activation energy (4.12 kcal/mol). Therefore, we are justified in making an additional comparison, namely, using experimental activation energies to estimate experimental binding energies for the ‡a site by approximately equating the

TABLE IV. Binding energies (kcal/mol), hydrogen-nickel interatomic distance (Å), hydrogen height above the surface plane (Å), and hydrogen vibrational frequencies (cm^{-1}) calculated in this study for a moving ($N_p=36$) Ni(100) surface compared to experimental and calculated values from the literature. For results from the literature, experimental values are listed first, followed by calculated values in parentheses.

	Binding energy		$R_{\text{H-Ni}}$		$R_{\text{H-surf}}$		Frequencies	
Site	EAM5	Lit.	EAMS	Lit.	EAM5	Lit.	EAM5	Lit.
H(a)	64.76	64.4±0.6[a]	1.83	1.82–1.84[b]	0.50	0.5±0.1[b]	753	589[c]
		64.6±0.9[d]		1.9–2.0[e]		0.9–1.0[e]		597[a]
		(62)[f]		(1.78)[g]		(0.3)[g]		621[h]
		(62)[i]		(1.8)[i]		(0.32)[j]		(532)[k]
		(69)[g]		(1.91)[f]		(0.8)[i]		(588)[g]
		(79)[j]		(1.92)[i]				(613)[f]
								(637)[i]
								(686)[l]
								(726)[j]
							524	387[c]
								(645)[g]
‡a	60.76	(63)[g]	1.56		0.93		1270	(1428)[g]
		(77)[j]					449	
							292i	

[a] Christmann, Schober, Ertl, and Neumann, Ref. 42.
[b] Stensgaard and Jokobsen (D/Ni), Ref.48.
[c] Mårtensson, Nyberg, and Andersson, Ref. 51.
[d] Lapujoulade and Neil, Ref. 41.
[e] Rieder and Wilsch, Ref. 46.
[f] Nordlander, Holloway, and Norskov, Ref. 47.
[g] Upton and Goddard, Ref. 44.
[h] Andersson, Ref. 43.
[i] Norskov, Ref. 45.
[j] Umrigar and Wilkins, Ref. 49.
[k] Karlsson, Mårtensson, Andersson, and Nordlander, Ref. 50.
[l] Mattsson, Engberg, and Wahnström, Ref. 4.

activation energies to classical barrier heights. (Usually, this is not an accurate equation due to tunneling and zero-point effects,[16] of which the former may be the more serious limitation, but if we use high-temperature rate data, the tunneling effects should be negligible enough for us to make a reasonable estimation for the adsorption energy for a hydrogen atom at the ‡a site.) The highest-temperature measurements of the diffusion coefficients are those of George *et al.*[52] for the temperature range 223–283 K; they analyzed their data to obtain an activation energy of 4±0.5 kcal/mol. Taking this highest-temperature activation energy as the best experimental estimate of the classical barrier height and using it in conjunction with the experimental equilibrium binding energies available for the H(a) site (Table IV) yields an adsorption energy of a hydrogen atom at the ‡a site of 60.6±1.4 kcal/mol, with which the current calculations (60.8) are in very good agreement.

We note at this point that although the EAM5 parametrization seems to yield a very good potential-energy surface for the Ni(100) surface, it does not accurately reproduce several experimental quantities for the Ni(111) surface (especially activation energies and frequencies). Further, it still has some of the bulk property flaws that were present in EAM4. Specifically, the bulk modulus predicted by the elastic constants is still low compared to experiment, and the Cauchy discrepancy ($C_{12}-C_{44}$) is still negative, indicating that the curvature of the embedding function is negative at the bulk equilibrium density. As explained above, the present fitting procedure is especially designed to yield a useful representation of the potential and its first and second derivatives along the minimum-energy path for surface diffusion on the (100) crystal face and along the reaction path for the octahedral-to-tetrahedral site-to-site bulk diffusion, and we emphasize that it is not recommended for the (111) surface or for calculations of the equation of state or lattice modes of bulk nickel. A more globally accurate EAM parametrization wil be presented in later work and called EAM6.

B. Diffusion coefficients and transition temperature

The rate constants for the H diffusion process on Ni(100) at several different levels of theory were calculated at temperatures ranging from 40 to 1000 K using the POLYRATE (Ref. 12) code. Table V lists the diffusion coefficients for the CVT level (with no tunneling corrections) and CVT/SCTQ level as described in the previous section.

First, we compare the current results to previous experimental and theoretical results at temperatures in the range where tunneling does not appear to have a significant effect. Figure 4 is an Arrhenius plot of the diffusion coefficients in the range 200–400 K. The current results are in excellent agreement with the experimental results of George, DeSantolo, and Hall,[52] and Mullins *et al.*,[53] who measured the diffusion rate with laser-induced thermal desorption at several temperatures between 211 and 283 K at coverages ranging from $\theta=0.12$ to 1.00 (the current calculations all correspond to the single-adatom limit, i.e., $\theta\approx 0$). The results also agree excellently with the theoretical results of Mattsson, Engberg, and Wahnström,[4] who studied the process in the single-adatom limit with path-integral techniques with an EAM potential function and used numerical Monte Carlo techniques for tunneling corrections. The fact that the present semiclassical reaction-path calculations (which are a form of path-integral approximation) agree well with the quantum Monte Carlo path-integral calculations is very encouraging for future applications of both methods.

TABLE V. CVT (no tunneling), and CVT/SCTQ diffusion coefficients (cm^2/s) for H on a moving ($N_p=36$) Ni(100) surface as functions of temperature. Powers of 10 are in parentheses.

T (K)	CVT	CVT/SCTQ
40	9.42(−26)	5.66(−15)
45	2.77(−23)	5.87(−15)
50	2.64(−21)	6.37(−15)
55	1.11(−19)	7.52(−15)
60	2.53(−18)	1.01(−14)
70	3.47(−16)	3.18(−14)
80	1.42(−14)	2.08(−13)
100	2.65(−12)	1.08(−11)
120	8.91(−10)	2.33(−10)
200	1.10(−7)	1.67(−7)
250	9.55(−7)	1.33(−6)
300	4.05(−6)	5.18(−6)
400	2.45(−5)	2.91(−5)
500	7.18(−5)	8.17(−5)
600	1.46(−4)	1.63(−4)
800	3.57(−4)	3.83(−4)
1000	6.15(−4)	6.51(−4)

The agreement with previous work at high temperature is very encouraging, but we will focus discussion on the low-temperature results for which tunneling is very important. We notice immediately that at very low temperatures (below 70 K), the diffusion coefficient is approximately independent of temperature, consistent with recent experimental and theoretical findings.[1–4] We define a transition temperature, T_{tr}, as the temperature below

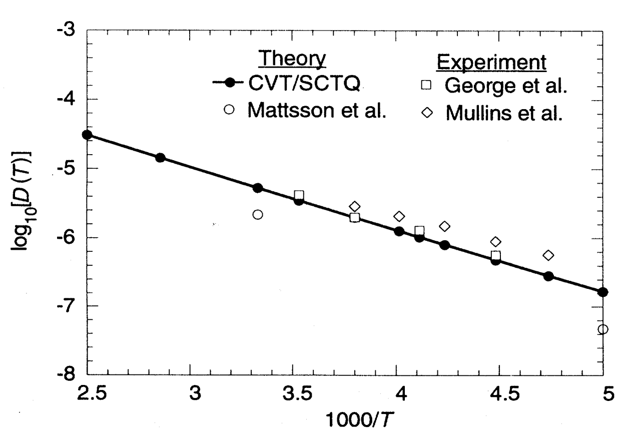

FIG. 4. Arrhenius plot of CVT/SCTQ diffusion coefficients calculated over the range 200–400 K and compared to previous experimental (Refs. 52 and 53) and theoretical (Ref. 4) results.

which this approximate temperature-independence sets in.

To obtain a precise analytical definition of the transition temperature, it is helpful to make two simplifying approximations. To motivate these, we consider Fig. 5, which is an Arrhenius plot of three sets of CVT/SCTQ diffusion coefficients, each at a different level of approximation. The first set, represented by circles, are the diffusion coefficients on a Ni(100) surface with $N_p=36$ calculated using the WKB approximations to the energy levels, E_v^R, i.e., the full high-level results given in Table V. The second set, represented by squares, are the diffusion coefficients on a Ni(100) surface with $N_p=36$ calculated using the harmonic approximation to the energy eigenstates [Eqs. (12) and (13)]. We note, very importantly, that using the harmonic energy levels is *not* a trivial approximation. Table VI gives the energy well eigenstates calculated by both the WKB and harmonic approximations. An extremely important difference between the two sets of energy levels is that the energy separation between E_0^R and E_1^R is much larger in the harmonic approximation than in the WKB approximation. This has the effect, which will be demonstrated shortly but can be seen in Fig. 5, of causing the Arrhenius plot to level off more dramatically below the transition temperature. However, the harmonic results are qualitatively similar to the first set of results in terms of the transition temperature, i.e., both sets of data appear to begin to level off at roughly the same temperature (slightly below 70 K). Thus, one simplifying approximation we will make in the following analysis of the transition temperature is the harmonic approximation. The reason for making this simplification is that the harmonic approximation gives analytical expressions for the energy eigenstates, which will allow us to present an analytical expression for the transition temperature. The third set of results in Fig. 5, represented by diamonds, are the diffusion coefficients on a *rigid* Ni(100) surface ($N_p=0$) again using the harmonic approximations to the energy eigenstates. We note that these results are nearly quantitatively identical to the second set of results, indicating that lattice motion has very little effect on the diffusion coefficients. Thus our analytic analysis of the transition temperature will assume a rigid lattice. The reason for making this simplification is that on a rigid surface, the double minimum seen in Fig. 2 does not occur. Since $N_p=0$, there are only two vibrational normal modes plus the mode corresponding to the reaction coordinate, all of which are high-frequency modes due to hydrogenic motion. Therefore, since there are no low-frequency modes corresponding to lattice motion, the mode corresponding to the reaction coordinate is the same mode over the entire course of the reaction resulting in a monotonic V_a^G from $s=0$ to s^R. As a result, $\bar{\upsilon}_F^R$ in Eqs. (11) and (12) equals $\bar{\upsilon}_3^R$, so the harmonic effective potential reduces to

$$V_{\text{eff}}(s)=V_a^G(s=s^R)+\tfrac{1}{2}f_3(s-s^R)^2\ , \tag{28}$$

which much more accurately represents the entire V_a^G curve away from $s=s_*^{\text{CVT}}$, and the energy eigenstates are

$$E_v^R=V_a^G(s=s^R)+(v+\tfrac{1}{2})hc\bar{\upsilon}_3^R\ . \tag{29}$$

TABLE VI. Energy levels, E_v^R (kcal/mol), with respect to $V_{\text{MEP}}(s=s^R)$, calculated using the WKB and harmonic approximations to the reaction-path mode. Only levels below $V_a^{\text{AG}}=37.98$ kcal/mol are quantized.

v	E_v^R(WKB)	E_v^R(harmonic)
0	34.00	34.10
1	34.90	35.59
2	35.84	37.09
3	36.68	
4	37.40	
5	37.94	

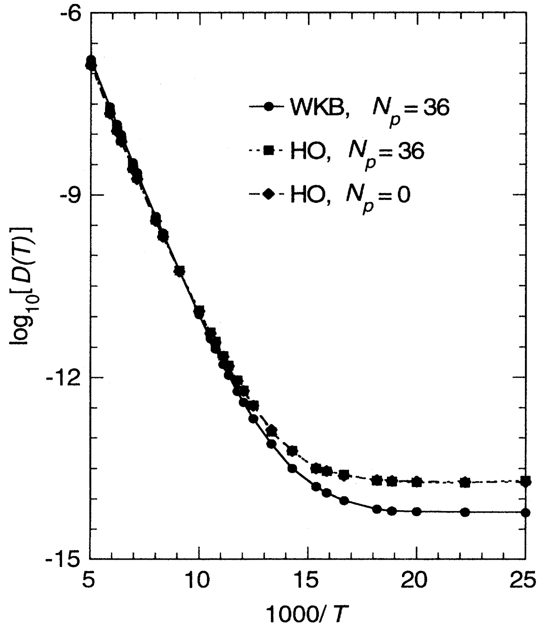

FIG. 5. Comparison of diffusion coefficients calculated at three levels of approximation. The circles are the high-level results given in Table V. The squares are values determined by making a harmonic approximation to the reaction-path mode. The diamonds are values determined by making a harmonic approximation to the reaction-path mode and using a rigid ($N_p=0$) Ni surface.

Making the simplifications described above, we can understand the origin of the transition temperature from Eqs. (2) and (6). At very low temperatures, only the ground state of the well is significantly populated, so only the E_0^R term in Eq. (6) remains. Integrating the denominator of Eq. (6) and keeping only E_0^R terms yields the following harmonic approximation to the transmission coefficient:

$$\kappa^{\mathrm{CVT/QG}}(T)=\frac{hc\bar{\upsilon}_F^R P^G(E_0^R)\exp\left[\dfrac{-E_0^R}{k_BT}\right]}{k_BT\exp\left[\dfrac{-V_a^G[s_*^{\mathrm{CVT}}(T)]}{k_BT}\right]} . \tag{30}$$

Recall that the CVT/SCTQ rate constant is a product of the semiclassical CVT rate constant and the ground-state transmission coefficient. So upon combining Eqs. (30) and (2) and rearranging, the CVT/SCTQ rate constant at low temperature becomes, in the harmonic approximation,

$$\begin{aligned} k^{\mathrm{CVT/SCTQ}}(T_{\mathrm{low}}) &= \sigma c\bar{\upsilon}_3^R P^G(E_0^R)\frac{Q^{\mathrm{CVT}}(T_{\mathrm{low}})}{Q^R(T_{\mathrm{low}})} \\ &\times\exp\left[\frac{V_a^G(s_*^{\mathrm{CVT}}(T_{\mathrm{low}}))-E_0^R-V_{\mathrm{MEP}}^{\mathrm{CVT}}(T_{\mathrm{low}})}{k_BT_{\mathrm{low}}}\right], \end{aligned} \tag{31}$$

where T_{low} denotes a low temperature. We use an independent normal-mode approximation, and the harmonic partition functions can be represented as a product over the individual mode partition functions:

$$Q(T)=\prod_{m=1}^{3}\frac{\exp\left[-\dfrac{1}{2}\dfrac{hc\bar{\upsilon}_m}{k_BT}\right]}{1-\left[\exp\left[-\dfrac{hc\bar{\upsilon}_m}{k_BT}\right]\right]} , \tag{32}$$

where m runs over all modes ($M=3$) for $Q^R(T)$ and over all modes orthogonal to the reaction coordinate ($M=2$) for $Q^{\mathrm{CVT}}(T)$. For $Q^R(T)$, the frequencies, $\bar{\upsilon}_m$, are just the frequencies of the reactant vibrations, $\bar{\upsilon}_m^R$, so the exponent numerator of Eq. (32) can be expressed in terms of the total zero-point energy of the reactants, which is E_0^R. Therefore, $Q^R(T)$ becomes

$$Q^R(T)=\exp\left[-\frac{E_0^R}{k_BT}\right]\prod_{m=1}^{3}\left\{1-\exp\left[-\frac{hc\bar{\upsilon}_m^R}{k_BT}\right]\right\} . \tag{33}$$

For $Q^{\mathrm{CVT}}(T)$, the frequencies are those orthogonal to the reaction path at s_*^{CVT}, i.e., $\bar{\upsilon}_m^{\mathrm{CVT}}$. Rearranging Eq. (3), $\varepsilon_{\mathrm{int}}^G(s_*^{\mathrm{CVT}}(T))=V_a^G(s_*^{\mathrm{CVT}}(T))-V_{\mathrm{MEP}}^{\mathrm{CVT}}(T)$, and $Q^{\mathrm{CVT}}(T)$ becomes, from Eq. (32),

$$\begin{aligned} Q^{\mathrm{CVT}}(T) &= \exp\left[-\frac{V_a^G(s_*^{\mathrm{CVT}}(T))-V_{\mathrm{MEP}}^{\mathrm{CVT}}(T)}{k_BT}\right] \\ &\times\prod_{m=1}^{2}\left\{1-\left[\exp\left[-\frac{hc\bar{\upsilon}_m^{\mathrm{CVT}}}{k_BT}\right]\right]\right\} . \end{aligned} \tag{34}$$

At very low temperatures, the products in Eqs. (33) and (34) approach unity, so the ratio of partition functions in Eq. (31) can be approximated at low temperature as

$$\frac{Q^{\mathrm{CVT}}(T_{\mathrm{low}})}{Q^R(T_{\mathrm{low}})} \approx\exp\left[-\frac{V_a^G(s_*^{\mathrm{CVT}}(T_{\mathrm{low}}))-V_{\mathrm{MEP}}^{\mathrm{CVT}}(T_{\mathrm{low}})-E_0^R}{k_BT_{\mathrm{low}}}\right] . \tag{35}$$

Substituting Eq. (35) into Eq. (31), we arrive at the final expression for the low-temperature limit (i.e., the point at which only the ground state, E_0^R, is populated) of the CVT/SCTQ rate constant in the harmonic approximation:

$$k^{\mathrm{CVT/SCTQ}}(T_{\mathrm{low}})\approx\sigma c\bar{\upsilon}_3^R P^G(E_0^R) , \tag{36}$$

and from Eq. (1),

$$D(T_{\mathrm{low}})\approx\frac{\lambda^2}{2d}\sigma c\bar{\upsilon}_3^R P^G(E_0^R) . \tag{37}$$

Equation (37) is temperature independent, giving the physical explanation for the low-temperature results in Fig. 5, i.e., the low-temperature limit is reached when only the ground state is populated. Recall from Table VI that the energy separation between the ground and first-excited states is larger in the harmonic approximation than in the WKB approximation. As a result, the ground state becomes dominant in the harmonic approximation at a higher temperature than in the WKB approximation, which causes the harmonic Arrhenius plot to level off faster than the WKB Arrhenius plot as seen in Fig. 5. We stress again, however, that since Eq. (37) was derived harmonically, E_0^R in that equation is the harmonic ground-state energy. Therefore, it does not give a particularly accurate estimation of the low-temperature limit to the diffusion coefficient calculated with the WKB energy levels. Extending the above treatment to the WKB method is difficult because there are no generic analytical expressions for the energy eigenstates in this method. Using Eqs. (8) and (9) for the energy eigenstates and energy separations yields the following approximate expression for the low-temperature limit in the WKB approximation:

$$D(T_{\mathrm{low}},\mathrm{WKB})\approx\frac{\lambda^2}{2d}\frac{\left[\left.\dfrac{dE_{v,\mathrm{WKB}}^R}{dv}\right|_{v=0}\right]\sigma P^G(E_{0,\mathrm{WKB}}^R)}{h} , \tag{38}$$

where $(dE_{v,\mathrm{WKB}}^R/dv)|_{v=0}$ is calculated in Eq. (9), and $E_{0,\mathrm{WKB}}^R$ is the ground-state WKB energy level of the reaction-path mode. Using the calculated values for $(dE_{v,\mathrm{WKB}}^R/dv)|_{v=0}$, $E_{0,\mathrm{WKB}}^R$, and $P^G(E_{0,\mathrm{WKB}}^R)$ of 0.88 kcal/mol, 34.00 kcal/mol, and 9.68×10^{-13}, respectively, yields $D(T_{\mathrm{low}})=5.54\times10^{-15}$ as the low-temperature limit to the diffusion coefficient in the WKB approximation, consistent with the results in Table V and Fig. 5, indicating that we have very nearly reached the low-temperature limit to the diffusion coefficient.

Even though Eq. (37) is derived harmonically, and is therefore not quantitatively accurate for the WKB low-temperature limit, it will still be useful in deriving an analytical expression for the transition temperature, because, as mentioned, the harmonic and WKB results *begin* to level off at roughly the same temperature. Therefore, in order to obtain an analytical expression for the transition temperature in terms of a concise number of well-defined quantities, we will continue to use Eq. (37) for the derivation. To get a quantitative grasp on the transition temperature, we examine what the low-temperature limit of the rate constant would look like if we included excited-state terms. Following the same steps as above with the inclusion of excited-state terms E_1^R and E_2^R in Eq. (6), the low-temperature diffusion coefficient becomes, in the harmonic approximation,

$$D(T_{\text{low}}) \approx \sum_{v=0}^{2} \left[\frac{\lambda^2}{2d} \sigma c \bar{v}_3^R P^G(E_v^R) \exp\left[\frac{-vhc\bar{v}_3^R}{k_B T_{\text{low}}} \right] \right] . \tag{39}$$

For Eq. (39) to lose its temperature dependence and reduce to Eq. (37), the $v=1$ and 2 terms in the summation must be negligible compared to the $v=0$ term. Figure 6 is a plot of the individual terms of the summation in Eq. (39), using the SCTQ calculated values for $P^G(E_v^R)$, along with the full summation and the full calculated diffusion coefficient (Table V) in the range $T=40$–100-K. In the region of the transition temperature, the $v=2$ term makes such a small contribution to the sum that the summation can be represented by two terms, yielding

$$D(T_{\text{low}}) \approx \frac{\lambda^2}{2d} \sigma c \bar{v}_3^R \left[P^G(E_0^R) + P^G(E_1^R) \exp\left[\frac{-hc\bar{v}_3^R}{k_B T_{\text{low}}} \right] \right] . \tag{40}$$

Two factors cause the low-temperature results calculated by Eq. (39) to deviate slightly from the full calculated values at the higher temperatures of this range. First, the approximation made in Eq. (35) begins to fail because the denominators of the partition functions begin to deviate from unity. Second, the continuum of states above V_a^{AG} in the numerator of Eq. (6) begins to become more populated, thus making the contribution of these states to the diffusion coefficient non-negligible. For the low-temperature region, however, Eq. (39) is an excellent approximation, and for purposes of discussion of the transition temperature region, Eq. (40) represents the diffusion coefficient very accurately.

The precise identification of the transition temperature is a matter of definition. Clearly, from Eqs. (39) and (40) and Fig. 6, the diffusion coefficient does not become truly temperature independent until $T=0$ K, because of all nonzero temperatures, excited states still make some contribution (albeit vanishingly small at very low T) to the diffusion coefficient. Therefore, to define the transition temperature as the point at which the diffusion coefficient is fully temperature independent is pointless. Instead, we want to define the transition temperature in such a way that it can relate to visual observables of the Arrhenius plot. In Fig. 6, the Arrhenius plot is approximately linear above 85 K and approximately horizontal below 55 K, so the transition temperature should be defined somewhere within this range. A suitable quantitative definition for the transition temperature is the temperature at which the Arrhenius plot reaches maximum curvature, which occurs when the third derivative of the logarithm of the diffusion coefficient with respect to $1/T$ is zero. Solving for T in the expression

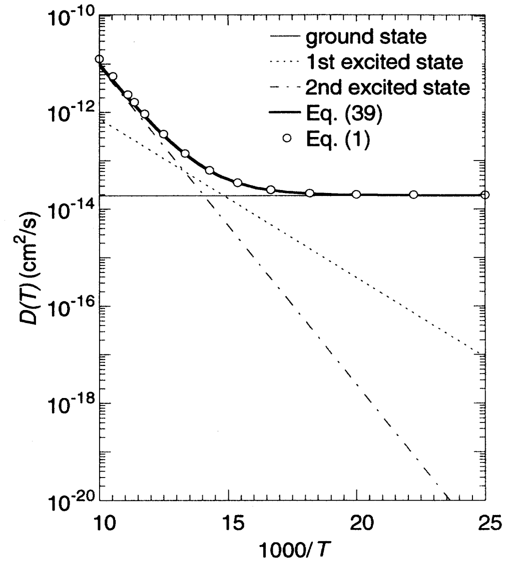

FIG. 6. Individual terms in the summation for the low-temperature harmonic approximation to the diffusion coefficient, Eq. (39), using the true adiabatic potential-energy curve to calculate transmission probabilities. The heavy solid line is the full summation, and white circles are the full CVT/SCTQ diffusion coefficient calculated for the current work using the ground-state transmission coefficient in Eq. (6) and not making the approximation of Eq. (35). The other three curves are terms in Eq. (39).

$$\frac{d^3\{\log_{10}[D(T_{\text{low}})]\}}{d(1/T)^3} = 0 , \tag{41}$$

with $D(T_{\text{low}})$ from Eq. (40) yields

$$T_{\text{tr}} = \frac{-hc\bar{v}_3^R}{k_B \ln\left[\dfrac{P^G(E_0^R)}{P^G(E_1^R)} \right]} . \tag{42}$$

At this point, Eq. (42) contains transmission probabilities, limiting its usefulness for experimentalists, because these are not measurable quantities. To develop an analytical expression for the transition temperature in terms of a small number of parameters of the system, we make a further simplification that the V_a^G curve, through which the particle is tunneling, can be represented by a parabola. We then follow the treatment of a previous study[54] to get approximations for these transmission probabilities. For a parabola, $P^G(E)$ can be approximated as[55]

$$P^G(E) = \frac{1}{1+\exp[\alpha(V_0 - E)]} , \tag{43}$$

where V_0 is the adiabatic barrier height, E is the energy at which tunneling occurs with respect to the adiabatic zero, and

$$\alpha = \frac{2\pi}{hc|\bar{v}^{\ddagger}|} \tag{44}$$

where $|\bar{v}^{\ddagger}|$ is the magnitude of the imaginary frequency at the top of the barrier in wave numbers. Substituting Eq. (43) into Eq. (42) yields, after some algebra,

$$T_{\text{tr}} = \frac{hc|\bar{v}^{\ddagger}|}{2\pi k_B} \; . \tag{45}$$

Equation (45) is a very important result because it depends only upon the magnitude of the imaginary frequency at the top of the barrier, $|\bar{v}^{\ddagger}|$.

This result is not immediately obvious. One's instinct is that the transition temperature would be directly proportional to the frequency of the reaction path, $\bar{v}_3^R$, because this frequency is proportional to the separation of the energy levels [see Eq. (13)]. As $\bar{v}_3^R$ decreases, the energy-level separation decreases, and the point at which temperature independence begins to set in (i.e., the point at which only the ground state is significantly populated), would have to decrease to a lower temperature. This is, in fact, true. However, recall that Eq. (45) is defined as the point of maximum curvature of the Arrhenius plot. At very low values of $\bar{v}_3^R$, the temperature at which temperature independence fully sets in indeed becomes very low because the shift in the slope of the Arrhenius plot becomes very spread out. However, even though this spreading out of the transition causes the actual point of maximum curvature (the transition temperature) to become less visibly defined, it remains relatively constant.

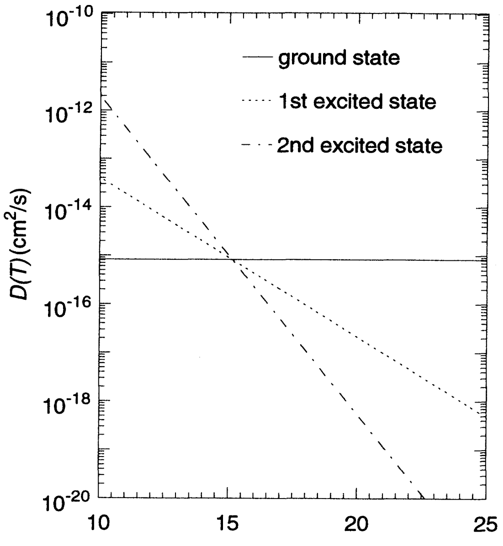

FIG. 7. Individual terms in the summation for the low-temperature harmonic approximation to the diffusion coefficient, Eq. (39), using the parabolic approximation to the adiabatic potential-energy curve to calculate transmission probabilities.

To better understand, then, why $|\bar{v}^{\ddagger}|$ should have an effect on the transition temperature, it is helpful to evaluate the transition temperature in another way. For an arbitrary value of $\bar{v}_3^R$, the summation in Eq. (39) is over all states. Making the parabolic approximation for $P^G(E)$, Eq. (39) becomes, after some algebra,

$$D(T_{\text{low}}) = \frac{\lambda^2}{2d}\sigma c \bar{v}_3^R \exp(-\alpha E_a) \times \sum_{v=0}^{\infty} \left\{ \exp\left[hc\bar{v}_3^R \left[\alpha - \frac{1}{k_B T_{\text{low}}} \right] \right] \right\}^v \; . \tag{46}$$

Equation (46) can be represented by a converging geometric series if $\alpha < (1/k_B T_{\text{low}})$, but the series diverges if $\alpha > (1/k_B T_{\text{low}})$. Now, to clarify, consider the lower limit of $\bar{v}_3^R$, in which the energy spacings of the bound states approach zero, yielding an infinite number of bound states. If the parabolic approximation, Eq. (43), for $P^G(E)$ is made, it can be shown (see Appendix B) that the ratio of contributions to the low-temperature diffusion coefficient, Eq. (39), of any two successive energy eigenstates is a constant. Therefore, when this ratio equals 1, all contributions are equal. This can be seen for the current system in Fig. 7, which shows the individual contributions to the low-temperature diffusion coefficient using the parabolic approximation for the $P^G(E_v^R)$ values. [Note that in Fig. 6, which uses the exact SCTQ calculated $P^G(E_v^R)$ values, the contributions do not exactly intersect. This is because the true V_a^G is not a true parabola. At this point it becomes important to note that the individual contributions differ by about an order of magnitude from Figs. 6 to 7. This is because the approximation in Eq. (43) is less accurate for processes, such as the current one, with low barrier heights. However, the errors are in the same direction and of about the same size for $P^G(E_0^R)$ and $P^G(E_1^R)$, and they cancel out when used in Eq. (45), making the latter equation accurate.] Below the temperature at which all state contributions are equal, the sum of the individual state contributions (i.e., the diffusion coefficient) converges. Above this temperature, the sum diverges. Therefore, when $\alpha = (1/k_B T_{\text{low}})$, the individual contributions are equal. Solving for T in this expression yields Eq. (45). This demonstrates that the point of maximum curvature on the Arrhenius plot corresponds to the temperature at which all individual state contributions (in the parabolic approximation) are equal. The magnitude of the frequency at the saddle point, $|\bar{v}^{\ddagger}|$, is related to the width of the barrier. Therefore, when this frequency increases, the width of the barrier decreases, making it easier for a particle to tunnel through the barrier at low energy, thus making its contribution to the diffusion coefficient larger. As a result, the temperature at which the contributions are equal becomes higher, thus raising the transition temperature.

To determine $|\bar{v}^{\ddagger}|$ for this process, the V_a^G curve from $s = -1.2$ to $s = 1.2$ Å (where $s^R \approx -1.5$ Å) was fit to a parabola,

$$V_a^G(s) = V_0 - \tfrac{1}{2}\mu(2\pi c|\bar{v}^{\ddagger}|)^2 s^2 \; , \tag{47}$$

where again μ is the scaling reduced mass of the system (1 amu). Solving for the magnitude of the imaginary frequency in Eq. (47) yields $|\bar{v}^{\ddagger}|=288\ \mathrm{cm}^{-1}$. Using this value in Eq. (45) gives a transition temperature of 66 K, which agrees very well with the high-level results in Fig. 5. Alternatively, if we chose to use $V_{\mathrm{MEP}}(s)$ to make this calculation, the results would be similar. Computing the second derivative of $V_{\mathrm{MEP}}(s)$ at its maximum yields $|\bar{v}^{\ddagger}|=292\ \mathrm{cm}^{-1}$ (see imaginary frequency for the $\ddagger a$ site in Table IV), resulting in a nearly identical transition temperature.

We remind the reader here that the derivation of Eq. (45) involved several simplifications, which affected the quantitative values of the diffusion coefficients. As a result, we do not recommend Eqs. (37), (39), (40), or (46) as extremely accurate approximations to the low-temperature limit to the diffusion coefficient (although they are reasonably accurate within one or two orders of magnitude). Instead, we offer the values given in Table V as our most accurate approximations to the diffusion coefficients. They were calculated using the WKB approximation to the reaction-path mode, used a moving Ni surface with $N_p=36$, and used the true adiabatic potential-energy curve to calculate transmission probabilities. However, the three main simplifications used to derive Eq. (45) (harmonic approximation to the reaction-path mode, rigid surface, and parabolic approximation of the V_a^G for transmission probability calculations) do not affect the qualitative nature of the transition to temperature independence as it has been defined in this paper. Hence, Eq. (45) gives a very good approximation to the transition temperature. As a further test, we also applied this treatment to H diffusion on Cu(100) with CVT/SCTQ tunneling calculations[56] and found Eq. (45) to produce accurate results for that system as well. [For the approximate potential function used in the H/Cu(100) studies, the transition temperature determined by Eq. (45) is 106 K, and this result is visually consistent with an Arrhenius plot of the diffusion coefficients from those studies.] We therefore conclude that this equation is useful for correlating results on different systems.

It is also of interest to relate T_{tr} to the EAM5 functions and parameters. Since T_{tr} is a function of the imaginary frequency at the saddle point, we varied the parameters in the potential-energy functions and determined which of the EAM5 parameters most influence this frequency. While no one parameter or combination of parameters is able to *substantially and exclusively* affect $|\bar{v}^{\ddagger}|$, the pair potential parameters, particularly Z_0, a, and b, tend to affect it with the least damage to the other energetics of the system. In particular, $|\bar{v}^{\ddagger}|$ increases with decreasing a or increasing Z_0 or b. The embedding energy parameters (α_H and β_H) tend to affect binding energies and equilibrium heights above the surface more than $|\bar{v}^{\ddagger}|$ and the other frequencies.

As a final note on the interpretation of the transition temperature, previous work[1-3] has suggested that this temperature represents a transition from over-barrier activated diffusion to tunneling diffusion. To better understand the transition temperature and evaluate this interpretation, we define a quantity, $F_{\mathrm{tun}}(T)$, as the fraction of the process that occurs by a tunneling mechanism,

$$F_{\mathrm{tun}}(T)=\frac{D_{\mathrm{tun}}(T)}{D(T)}\ , \tag{48}$$

where $D(T)$ is the full calculated diffusion coefficient, Eq. (1), and $D_{\mathrm{tun}}(T)$ is the diffusion coefficient calculated using only the bound energy states below V_a^{AG}. At these energies the diffusion proceeds by a tunneling mechanism, and in the energy continuum above V_a^{AG}, it proceeds by an activated over-barrier mechanism. $D_{\mathrm{tun}}(T)$ is calculated by using only the summation in the numerator of Eq. (6) for the ground-state transmission coefficient. Figure 8 is a plot of $F_{\mathrm{tun}}(T)$ over a temperature range from 40 to 200 K. At the transition temperature, 66 K, $F_{\mathrm{tun}}(T)$ is about 96%, and tunneling still dominates well above this temperature. We conclude, therefore, that this temperature does not represent a dramatic shift from activated to tunneling diffusion. Instead, from the discussion below Eq. (46), it represents the temperature at which all energy eigenstates (ground and excited) of the reaction-path mode contribute to the diffusion coefficient about equally.

At this point it is useful to compare the calculated low-temperature diffusion coefficients and transition temperatures to previous work. Figure 9 is an Arrhenius plot of the CVT/SCTQ diffusion coefficients along with previous experimental and theoretical results that have explored the low-temperature region. Lin and Gomer[1] used the field-emission fluctuation technique[57] and Zhu and co-workers[2,3] used linear optical diffraction techniques to examine this process at low temperatures. The Mattsson, Engberg, and Wahnström results are from the study[4] discussed above with regard to higher temperatures in Fig. 4. The latter study also included the temperature range down to 25 K, but to preserve the resolution of the Arrhenius plot and enable adequate visual comparison to all previous results, only results down to 40 K are shown in Fig. 9. The values for the diffusion coefficients plotted are from the $\theta=0.9$ coverage experiments of Zhu

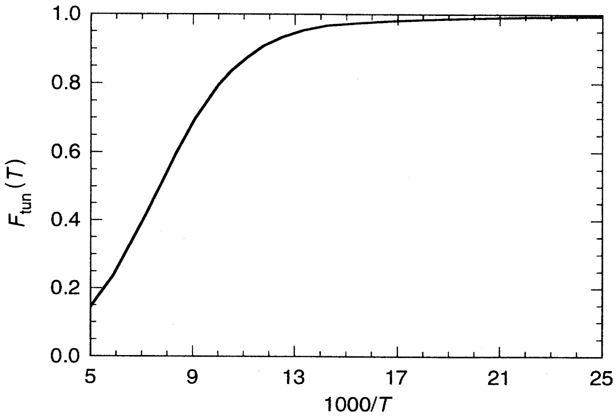

FIG. 8. Percentage of diffusion process occurring by a tunneling mechanism, $F_{\mathrm{tun}}(T)$, over the range $T=40$–200 K.

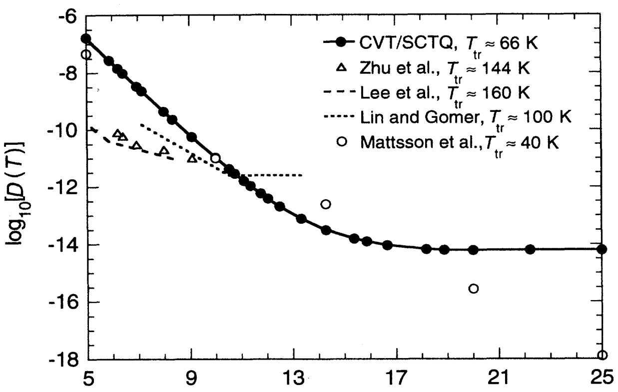

FIG. 9. Arrhenius plot of CVT/SCTQ diffusion coefficients for 40–100 K compared to previous experimental and theoretical results. The locations of the transition temperatures determined in each study are compared in the label.

et al.[2] For the $\theta = 0.7$ coverage experiments of Lee *et al.*,[3] a two-part linear plot is derived from the diffusivities (Arrhenius preexponential factors) and activation energies in two temperature ranges (120–160 K and 160–200 K) reported in Ref. 3. For the Lin and Gomer experiments, the high-temperature region of the plot is derived from the preexponential factors and activation energies, and the low-temperature regions are estimated from the fits for this data in Ref. 1. The calculations of Mattson, Engberg, and Wahnström[4] like ours, are for $\theta \approx 0$. It is possible that the comparison of our results to previous experiments suffers from the fact that the experiments are performed at nonzero coverages and our calculations are in the single-adatom limit. However, Lin and Gomer[1] very thoroughly tested the coverage dependence of this diffusion process, and they saw very minimal variation of Arrhenius activation energies and preexponential factors and transition temperature locations over a coverage range from θ equals 0.25 to θ equals 0.95. Lee *et al.*[3] reported similar weak coverage dependence of the diffusion coefficients for θ from 0.3 to 0.8. We conclude, then, that the extrapolation to $\theta = 0$ is probably valid, at least for semiquantitative and qualitative interpretation of the experiments.

The CVT/SCTQ diffusion coefficients are in reasonably good agreement with the experimental quantities, but the low-temperature results are somewhat difficult to compare due to various locations of the transition temperature, i.e., since the experimental transition temperatures are higher than our calculated value, the diffusion coefficients tend to become independent of temperature at higher temperatures than the present calculated values. As a result, at very low temperatures, the diffusion coefficients are in disagreement. We note here that although the 144- and 160-K transition temperatures of Zhu and co-workers[2,3] are indeed transition temperatures as they have been defined in this paper (i.e., they represent the temperature at which curvature of the Arrhenius plot is a maximum), the diffusion coefficients do not become independent of temperature below these temperatures. Instead, the activation energies (i.e., the slopes of the Arrhenius plots) merely shift to lower (nonzero) values at these temperatures. This indicates, from previous discussion, that excited states are still substantially populated. [It would be interesting to see if at very low temperatures, the linear optical diffraction experiments would reveal a more complete temperature independence. This has, in fact, been seen in very recent linear optical diffraction studies by the same research group for H on Ni(111).[58]] In contract, the diffusion coefficients measured by Lin and Gomer[1] become temperature indepen-

TABLE VII. Activation energies (E_a, kcal/mol) and preexponential factors (D_0, cm^2/s) for surface diffusion of H on Ni(100) for several temperature ranges compared to experimental values. Powers of 10 are in parentheses.

	E_a		D_0	
T (K)	CVT/SCTQ	Experiment	CVT/SCTQ	Experiment
40–50	0.050		1.05 (−14)	
55–65	0.54		1.06 (−12)	
70–80	2.1		1.07 (−7)	
85–95	3.2		1.02 (−4)	
100–140	3.7	3.2[a]	1.55 (−3)	8. (−6)[a]
120–170	3.9	1.2[b]	2.81 (−3)	1.5 (−9)[b]
156–161	4.0	3.5[c]	3.38 (−3)	8. (−6)[c]
170–200	4.0	3.5[b]	4.30 (−3)	1.1 (−6)[b]
211–263	4.1	3.5±0.3[d]	4.97 (−3)	2.5 (−3)[d]
223–283	4.1	4±0.5[e]	5.35 (−3)	4.5 (−3)[e]
300–400	4.1		5.58 (−3)	

[a] Lin and Gomer, Ref. 1.
[b] Lee, Zhu, Deng, and Linke, Ref. 3.
[c] Zhu, Lee, Wong, and Linke, Ref. 2.
[d] Mullins, Roop, Costello, and White, Ref. 53.
[e] George, DeSantolo, and Hall, Ref. 52.

dent below the transition temperature of 100 K, indicating that below this temperature, only the ground state is significantly populated. This, in fact, is the physical significance of our transition temperature of 67 K. As a result, we are very encouraged by the location of our transition temperature compared to the 100-K value reported by Lin and Gomer, and we are not discouraged by the higher transition temperatures of Zhu and co-workers. The CVT/SCTQ transition temperature of roughly 67 K is, to our knowledge, the only theoretical approximation to predict a transition temperature so close to the experimentally reported values. The results of the path-integral studies by Mattsson, Engberg, and Wahnström showed the transition temperature to occur at about 40 K, somewhat low in comparison to experiment, and this low temperature is not shown in Fig. 9. The latter calculations made use of the original EAM potential-energy function [i.e., EAM1 (Ref. 5)]. Although the differences between EAM1 and EAM5 are certain to contribute slightly to the different transition temperature observed by Mattsson *et al.*, the energetics predicted by EAM1 and EAM5 for the process under consideration here are very quantitatively similar and unlikely to account for the nearly 30-K difference in the temperature at which excited states begin to become negligibly populated. The different dynamics methods are far more likely to be the primary cause of these conflicting results.

Finally, when the data in Figs. 4 and 9 are fit to the Arrhenius equation,

$$D(T)=D_0\exp\left[\frac{-E_a}{RT}\right] , \tag{49}$$

where R is the gas constant, the preexponential factors (diffusivities) and activation energies can be extracted and compared, and this is done in Table VII, where in each row the CVT/SCTQ values are obtained by fitting Eq. (49) to the calculated $D(T)$ values at two temperatures. The values are in very good agreement with those of Mullins *et al.* and George *et al.*, and they are in moderate agreement with those of Lin and Gomer and Zhu and co-workers. Again, however, direct comparisons of these quantities at specific temperatures are limited because of the various locations of the transition temperatures.

IV. SUMMARY

We have used an embedded atom method potential-energy function and small reaction-path-curvature multidimensional tunneling calculations with quantized reactant well states to calculate surface-diffusion coefficients for H on Ni(100). We find the energetics and dynamics to be for the most part in very good agreement with experiment. We present an interpretation of the transition temperature, and by using the harmonic-well and parabolic-barrier models, we presented a concise analytical approximation for this quantity that is dependent only upon the magnitude of the imaginary frequency associated with the top of the barrier.

ACKNOWLEDGMENTS

This work was supported in part by the National Science Foundation through Grant No. CHE89-22048.

APPENDIX A

This appendix explains how we obtained "experimental" values for the equilibrium dissociation energies, D_e, from available experimental quantities. The process we need to consider in order to calculate D_e values for comparison to the binding energies of an H atom at a surface minimum-energy site of fourfold symmetry [i.e., H(a)] in Table III is

$$\mathrm{H\cdot Ni(ad)}\rightarrow \mathrm{H}(g)+\mathrm{Ni}(s) . \tag{I}$$

The D_e value is the classical energy change in this process at 0 K. Thus, it excludes both zero point and thermal energy, i.e.,

$$D_e[\mathrm{H\cdot Ni(ad)}]=D_0[\mathrm{H\cdot Ni(ad)}]-\Delta E_{\mathrm{ZP}}(\mathrm{I}) , \tag{A1}$$

where D_0 is the thermodynamic dissociation energy at 0 K, E_{ZP} is zero-point energy, and $\Delta X(J)$ denotes the change in variable X during process J.

Consider the generic process:

$$A\rightarrow B . \tag{II}$$

The enthalpy change for a process (II) at temperature T and pressure P is

$$\Delta H_T(\mathrm{II})=\Delta E_T(\mathrm{II})+P\Delta V(\mathrm{II})\cong\Delta E_T(\mathrm{II})+RT\Delta n_g(\mathrm{II}) , \tag{A2}$$

where ΔE_T is the energy change for the process at temperature T, ΔV is change in volume, Δn_g is the change in moles of gas, and R is the gas constant. Note that

$$\Delta E_0=D_0 . \tag{A3}$$

Hence,

$$D_e=\Delta E_0(\mathrm{I})-\Delta E_{\mathrm{ZP}}(\mathrm{I}) . \tag{A4}$$

We will obtain ΔE_0(I) by combining thermodynamic data for two other processes:

$$2\mathrm{H\cdot Ni(ad)}\rightarrow \mathrm{H_2}(g)+2\mathrm{Ni}(s) \tag{III}$$

and

$$\mathrm{H_2}(g)\rightarrow 2\mathrm{H}(g) . \tag{IV}$$

This yields

$$\begin{aligned} D_e[\mathrm{H\cdot Ni(ad)}]&=\tfrac{1}{2}[\Delta E_0(\mathrm{III})+\Delta E_0(\mathrm{IV})]-\Delta E_{\mathrm{ZP}}(\mathrm{I})\\ &=\tfrac{1}{2}\{\Delta E_0(\mathrm{III})+D_0[\mathrm{H_2}(g)]\}-\Delta E_{\mathrm{ZP}}(\mathrm{I}) . \end{aligned} \tag{A5}$$

Since the experimentally available datum for process III is ΔH_T at a finite temperature, we note that

$$\Delta H_T(\mathrm{III})=\Delta E_0(\mathrm{III})+\Delta(PV)_T(\mathrm{III}) +E_T[\mathrm{H}_2(g)]-E_0[\mathrm{H}_2(g)] -2\Delta\varepsilon_T^{\mathrm{adatom}}(\mathrm{III})+\Delta\varepsilon_T^{\mathrm{lattice}}(\mathrm{III})\ , \tag{A6}$$

where $\Delta\varepsilon^{\mathrm{adatom}}$ and $\Delta\varepsilon^{\mathrm{lattice}}$ are the vibrational energy contributions of the adatom and lattice modes, respectively. We assume that $\Delta\varepsilon_T^{\mathrm{lattice}}(\mathrm{III})$ and the vibrational contribution to E_T-E_0 for $\mathrm{H}_2(g)$ are negligible, that $\Delta(PV)_T$ is primarily due to Δn_g, and that rotation and translation may be treated classically.[39] Then Eq. (A6) becomes

$$\Delta H_T(\mathrm{III})=\Delta E_0(\mathrm{III})+\tfrac{7}{2}RT-2\Delta\varepsilon_T^{\mathrm{adatom}}(\mathrm{III})\ . \tag{A7}$$

If we also assume that the phonon frequencies do not change appreciably upon desorption (our calculations with EAM5 confirm that this is a good assumption to within 0.1 kcal/mol), then Eq. (A5) becomes

$$D_e[\mathrm{H}\cdot\mathrm{Ni(ad)}]=\tfrac{1}{2}\{\Delta H_T(\mathrm{III})+D_0[\mathrm{H}_2(g)]-\tfrac{7}{2}RT\} +\Delta\varepsilon_T^{\mathrm{adatom}}(\mathrm{III})+\Delta\varepsilon_0^{\mathrm{adatom}}(\mathrm{I})\ . \tag{A8}$$

Letting the adatom frequencies in wave numbers be denoted by $\bar{v}_m$ with $m=1$, 2, 3 and making the harmonic approximation[39] yields

$$D_e[\mathrm{H}\cdot\mathrm{Ni(ad)}]=\tfrac{1}{2}\Delta H_T(\mathrm{III})+\tfrac{1}{2}D_0[\mathrm{H}_2(g)]-\tfrac{7}{4}RT+N_Ahc\sum_{m=1}^{3}\left[\frac{\bar{v}_m}{\exp(N_Ahc\bar{v}_m/k_BT)-1}+\frac{\bar{v}_m}{2}\right]\ , \tag{A9}$$

where N_A is Avagadro's number. The H_2 dissociation energy at 0 K including zero-point energy, $D_0[\mathrm{H}_2(g)]$, is known experimentally to be 103.25 kcal/mol,[40] and $\bar{v}_m$, $m=1$, 2, 3 are 605±16, 387, and 387 wave numbers.[51] Then, for each experimental value of $\Delta H_T(\mathrm{III})$ we can calculate $D_e[\mathrm{H}\cdot\mathrm{Ni(ad)}]$, and these values are listed in Table IV.

APPENDIX B

We need to show that by making the parabolic approximation for $P^G(E)$, Eq. (43), the ratio of the contributions of any two successive harmonic energy eigenstates to the low-temperature diffusion coefficient in Eq. (39) is constant. Therefore, we need to prove that the ratio of the contribution of state $(n+2)$ to that of state $(n+1)$ is equal to the ratio of the contribution of state $(n+1)$ to that of state n. From Eq. (39), we need to show

$$\frac{P^G(E_{n+2})\exp\left[\dfrac{-(n+2)hc\bar{v}^R}{k_BT}\right]}{P^G(E_{n+1})\exp\left[\dfrac{-(n+1)hc\bar{v}^R}{k_BT}\right]}=\frac{P^G(E_{n+1})\exp\left[\dfrac{-(n+1)hc\bar{v}^R}{k_BT}\right]}{P^G(E_n)\exp\left[\dfrac{-nhc\bar{v}^R}{k_BT}\right]}\ . \tag{B1}$$

Cross multiplying yields

$$P^G(E_{n+1})^G(E_{n+1})=P^G(E_{n+2})P^G(E_n)\ . \tag{B2}$$

Using the harmonic values, Eq. (13), for the energy separations, making the parabolic approximation, Eq. (35), and further assuming that $\exp[\alpha(V_0-E)]\gg 1$ for $E=E_n$, E_{n+1}, and E_{n+2} yields

$$\exp[2\alpha(E_n+hc\bar{v}^R-V_0)]=\exp[2\alpha(E_n+hc\bar{v}^R-V_0)]\ , \tag{B3}$$

which proves Eq. (B1).

---

[1] T.-S. Lin and R. Gomer, Surf. Sci. **225**, 41 (1991).

[2] X. D. Zhu, A. Lee, A. Wong, and U. Linke, Phys. Rev. Lett. **68**, 1862 (1992).

[3] A. Lee, X. D. Zhu, L. Deng, and U. Linke, Phys. Rev. B **46**, 15 472 (1992).

[4] T. R. Mattsson, U. Engberg, and G. Wahnström, Phys. Rev. Lett. **71**, 2615 (1993).

[5] M. Daw and M. Baskes, Phys. Rev. B **29**, 6443 (1984).

[6] D. G. Truhlar and B. C. Garrett, Acc. Chem. Res. **13**, 440 (1980).

[7] D. G. Truhlar and B. C. Garrett, Annu. Rev. Phys. Chem. **35**, 159 (1984).

[8] S. C. Tucker and D. G. Truhlar, in *New Theoretical Methods for Understanding Organic Reactions*, edited by J. Bertran and I. G. Csizmadia (Kluwer, Dordrecht, 1989), pp. 291–346.

[9] R. T. Skodje, D. G. Truhlar, and B. C. Garrett, J. Phys. Chem. **85**, 3019 (1981).

[10] R. T. Skodje, D. G. Truhlar, and B. C. Garrett, J. Chem. Phys. **77**, 5955 (1982).

[11] D. G. Truhlar, A. D. Isaacson, and B. C. Garrett, in *Theory of Chemical Reaction Dynamics*, edited by M. Baer (CRC, Boca Raton, FL, 1985), pp. 65–137.

[12] (a) D.-h. Lu, T. N. Truong, V. S. Melissas, G. L. Lynch, Y.-P. Liu, B. C. Garrett, R. Steckler, A. D. Isaacson, S. N. Rai, G. C. Hancock, J. G. Lauderdale, T. Joseph, and D. G. Truhlar, Comput. Phys. Commun. **71**, 235 (1992); (b) R. Steckler, W.-P. Hu, Y.-P. Liu, G. C. Lynch, B. C. Garrett, A. D. Isaacson, D.-h. Lu, V. S. Melissas, T. N. Truong, S. N. Rai, G. C. Hancock, J. G. Lauderdale, T. Joseph, and D. G. Truhlar, POLYRATE—version 6.1, University of Minnesota, Minneapo-

lis, 1994.

[13] Y.-P. Liu, G. Lynch, T. N. Truong, D.-h. Lu, D. G. Truhlar, and B. C. Garrett, J. Am. Chem. Soc. **115**, 2408 (1993).

[14] J. G. Lauderdale and D. G. Truhlar, Surf. Sci. **164**, 558 (1985).

[15] J. G. Lauderdale and D. G. Truhlar, J. Chem. Phys. **84**, 1843 (1986).

[16] S. E. Wonchoba and D. G. Truhlar, J. Chem. Phys. **99**, 9637 (1993).

[17] A. F. Voter and J. D. Doll, J. Chem. Phys. **80**, 5832 (1984).

[18] G. Wahnström and H. Metiu, Chem. Phys. Lett. **145**, 44 (1988); G. Wahnström, K. Haug, and H. Metiu, *ibid.* **148**, 158 (1988); K. Haug, G. Wahnström, and H. Metiu, J. Chem. Phys. **90**, 540 (1989).

[19] R. A. Marcus, J. Chem. Phys. **41**, 610 (1964).

[20] R. A. Marcus, J. Chem. Phys. **45**, 4493 (1966).

[21] I. Shavitt, J. Chem. Phys. **49**, 4048 (1968).

[22] D. G. Truhlar and A. Kuppermann, J. Am. Chem. Soc. **93**, 1840 (1971).

[23] B. C. Garrett, D. G. Truhlar, R. S. Grev, and A. W. Magnuson, J. Phys. Chem. **84**, 1730 (1980).

[24] B. C. Garrett and D. G. Truhlar, J. Phys. Chem. **83**, 2921 (1979).

[25] B. C. Garrett, N. Abusalbi, D. J. Kouri, and D. G. Truhlar, J. Chem. Phys. **83**, 2252 (1985).

[26] M. S. Daw, S. M. Foiles, and M. I. Baskes, Mater. Sci. Rep. **9**, 251 (1993).

[27] T. N. Truong, D. G. Truhlar, and B. C. Garrett, J. Phys. Chem. **93**, 8227 (1989).

[28] S. M. Foiles, M. I. Baskes, and M. S. Daw, Phys. Rev. B **33**, 7983 (1986).

[29] T. N. Truong and D. G. Truhlar, J. Phys. Chem. **94**, 8262 (1990).

[30] B. M. Rice, B. C. Garrett, M. L. Koszykowski, S. M. Foiles, and M. S. Saw, J. Chem. Phys. **92**, 775 (1990); **100**, 8556(E) (1994).

[31] C. Kittel, *Introduction to Solid State Physics,* 6th ed. (Wiley, New York, 1986).

[32] J. H. Rose, J. R. Smith, F. Guinea, and J. Ferrante, Phys. Rev. B **29**, 2963 (1984).

[33] G. Simmons and H. Wang, *Single Crystal Elastic Constants and Calculated Aggregate Properties: A Handbook* (MIT, Cambridge, MA, 1971).

[34] *Vacancies and Interstitials in Metals,* edited by A. Seeger, D. Schumacher, W. Schilling, and J. Diehl (North-Holland, Amsterdam, 1970), p. 36; H. Bakker, Phys. Status Solidi **28**, 569 (1968).

[35] R. A. Johnson, Phys. Rev. **145**, 423 (1965).

[36] A. A. Mamalui, T. D. Ostinskaya, V. A. Pervakov, and V. I. Khomkevich, Fiz. Tverd. Tela (Leningrad) **10**, 2892 (1968) [Sov. Phys. Solid State **10**, 2290 (1969)].

[37] W. Wycisk and M. Feller-Kniepmeier, J. Nucl. Mater. **69-70**, 616 (1978).

[38] *Metal Reference Book,* 5th ed., edited by C. J. Smith (Butterworths, London, 1976), p. 186.

[39] J. A. Fay, *Molecular Thermodynamics* (Addison-Wesley, Reading, MA, 1965).

[40] J. H. Noggle, *Physical Chemistry,* 2nd ed. (Scott, Foresman, and Co., Glenview, 1989).

[41] J. Lapujoulade and K. S. Neil, Surf. Sci. **35**, 288 (1973).

[42] K. Christmann, O. Schober, G. Ertl, and H. Neumann, J. Chem. Phys. **60**, 4528 (1974).

[43] S. Andersson, Chem. Phys. Lett. **55**, 185 (1978).

[44] T. H. Upton and W. A. Goddard, Phys. Rev. Lett. **42**, 472 (1979).

[45] J. K. Norskov, Phys. Rev. Lett. **48**, 1620 (1982).

[46] K. H. Rieder and H. Wilsch, Surf. Sci. **131**, 245 (1983).

[47] P. Nordlander, S. Holloway, and J. K. Norskov, Surf. Sci. **136**, 59 (1984).

[48] I. Stensgaard and F. Jakobsen, Phys. Rev. Lett. **54**, 711 (1985).

[49] C. Umrigar and J. W. Wilkins, Phys. Rev. Lett. **54**, 1551 (1985).

[50] P.-A. Karlsson, A.-S. Mårtensson, S. Andersson, and P. Nordlaner, Surf. Sci. **175**, L759 (1986).

[51] A.-S. Mårtensson, C. Nyberg, and S. Andersson, Surf. Sci. **205**, 12 (1988).

[52] S. M. George, A. M. DeSantolo, and R. B. Hall, Surf. Sci. **159**, L425 (1985).

[53] D. R. Mullins, B. Roop, S. A. Costello, and J. M. White, Surf. Sci. **186**, 67 (1987).

[54] R. T. Skodje and D. G. Truhlar, J. Phys. Chem. **85**, 624 (1981).

[55] E. C. Kemble, *The Fundamental Principles of Quantum Mechanics With Elementary Applications* (McGraw-Hill, New York, 1937), p. 109ff.

[56] S. Wonchoba, W. P. Hu, and D. G. Truhlar, in *Theoretical and Computational Approaches to Interface Phenomena* (Plenum, New York, in press).

[57] G. Mazenko, J. R. Banavar, and R. Gomer, Surf. Sci. **107**, 459 (1981).

[58] A. Lee, X. D. Zhu, A. Wong, L. Deng, and U. Linke, Phys. Rev. B **48**, 11 256 (1993).